Accepted Manuscript

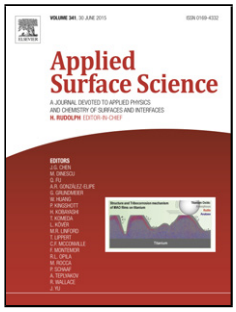

Title: PEO of pre-anodized Al-Si alloys: Corrosion properties and influence of sealings

Author: M. Mohedano E. Matykina R. Arrabal B. Mingo A. Pardo

PII: S0169-4332(15)00822-3
DOI: http://dx.doi.org/doi:10.1016/j.apsusc.2015.03.206
Reference: APSUSC 30083

To appear in: *APSUSC*

Received date: 14-10-2014
Revised date: 3-3-2015
Accepted date: 29-3-2015

Please cite this article as: M. Mohedano, E. Matykina, R. Arrabal, B. Mingo, A. Pardo, PEO of pre-anodized Al-Si alloys: Corrosion properties and influence of sealings, *Applied Surface Science* (2015), http://dx.doi.org/10.1016/j.apsusc.2015.03.206

Highlights:

- A356 gravity-cast and rheocast pre-anodized aluminium alloys were coated by PEO.

- Different sealing techniques were applied after the coating process.

- Iron-rich constituents of the substrate occlude the continuity of the porous anodic film.

- PEO coatings consisted of a mixture of α-Al_2O_3, γ-Al_2O_3 and mullite.

- Post-treatments improved both hydrophobic and corrosion properties.

PEO of pre-anodized Al-Si alloys: Corrosion properties and influence of sealings

M. Mohedano[a*], E. Matykina[b], R. Arrabal[b], B. Mingo[b], A. Pardo[b]

[a]Helmholtz Zentrum Geesthacht, Magnesium Innovation Centre, Institute of Materials Research, Max-Planck-Str. 1, D-21502 Geesthacht, Germany.

[b]Departamento de Ciencia de Materiales, Facultad de Ciencias Químicas, Universidad Complutense, 28040, Madrid, Spain.

[*]*Corresponding author. Tel: 494152871956; Fax: 494152871960*

E-mail: marta.mohedano@hzg.de

Abstract

Voltage-controlled PEO coatings were developed on A356 aluminum alloys (gravity-cast and rheocast) with a pre-anodized layer. The influence of the alloy manufacturing process and the effect of Si-rich phase on the structure and composition of the oxide layers were evaluated using SEM, EDS and XRD. The pre-anodized oxide layer preserves the microstructure of the substrate due to the presence of secondary phases that have a different behavior relative to the matrix during anodizing. PEO coatings consisted of a mixture of α-Al_2O_3, γ-Al_2O_3 and mullite. The corrosion behavior and the effectiveness of different sealing techniques based on salts of nickel, cobalt, cerium and phosphonic acid were also studied. Post-treatments improved the hydrophobic properties of the coatings and showed a beneficial effect, significantly increasing the coating impedance and thereby reducing the susceptibility to corrosion.

Keywords: Aluminum, Anodizing, PEO, Post-treatment, Corrosion.

1. Introduction

In the automotive industry, aluminium–silicon cast alloys have wide applications due to the combination of high strength over weight ratio and excellent fluidity and castability [1,2]. Over the last years, some efforts have been done to increase the efficiency of their production process which is long and energy wasting. Among all of them, a new industrial processing technique, called semisolid metal processing (SSM), has shown to be a good candidate to reduce the cost investment preserving or even improving the performance of the alloy. In case of A356 aluminum alloy, semisolid processed parts show less degree of porosity, increased ductility and higher resistance to pitting corrosion than the gravity-cast alloy [3-5]. Nevertheless, regardless of the manufacturing process, the corrosion and wear properties of Al-Si alloys need to be improved particularly under aggressive environment when longer warranty time and higher vehicle mileages are required [6].

Surface modification by conventional anodizing, commonly used for Al alloys, is not ideal in case of Al-Si alloys due to the presence of the silicon phase hindering the uniform growth of the anodic film [7-9]. Plasma Electrolytic Oxidation (PEO) is one of the alternative options to the traditional anodizing process of light alloys and aluminium alloys in particular. PEO involves anodic polarization of the alloy to voltages above the dielectric breakdown voltage, which generates short-lived plasma microdischarges across the growing oxide [10,11]. The oxide layers developed by PEO are hard, well-adherent to the substrate and improve both corrosion and wear properties [12].

In the particular case of Al and its alloys, PEO coatings usually show three different layers: i) a porous outer layer with low hardness and rich in the metastable phase γ-Al_2O_3 which represents between 5 - 30% of the coating thickness; ii) a compact and dense intermediate

layer with high wear resistance and rich in the phase α-Al_2O_3 which represents between 70 - 95% of the total coating thickness and (iii) sub-micron size amorphous barrier layer adjacent to the substrate [13,14]. For these coatings, a special microdischarge regime ("soft sparking") can be achieved controlling the intensity and lifetime of the discharges, and this regime has been reported to show a double beneficial effect in the coating development, decreasing the anomalous gas evolution of PEO process [15] and leading to the formation of thick, homogeneous and dense layers [16,17]. The transition to "soft sparking" occurs once a sufficient thickness of the coating has been achieved. For pure Al and commercial Al alloys, it has been demonstrated that the presence of pre-anodized porous layers of ~20-30 μm thickness promotes the transition to the micro-arc or "soft sparking" regime, leading to formation of thicker coatings with lower energy consumption [18,19]. In particular for Al-Si alloys, the difference in the oxidation rates of the Si-rich phase and Al-rich phase in the alloy matrix has been reported to have a detrimental effect on the structure of conventional PEO coatings [20-24]. In case of A356 aluminum alloy, the presence of pre-anodized porous layers leads up to 57% reduction of the energy consumption of voltage-controlled PEO process, compared with non-pre-anodized alloys [25]. However, the growth mechanism remains somewhat unclear and for the authors' knowledge there are no previous studies involving the effect of process manufacturing of Al-Si alloys in the formation of the pre-anodized layer and the posterior development of PEO coatings.

Regarding the corrosion performance, the unavoidable porous microstructure of PEO coated materials compromises their corrosion behavior, and post-treatments sealing techniques might be the solution to reduce their porosity by blocking the pores. A wide range of post-sealing processes have been developed for conventional anodizing, such as hot water, silicates, polymer solutions and sol-gel coatings [26-28]. Among all of them, the treatments based on

aqueous salt solutions such as nickel acetate, cerium nitrate and potassium permanganate have shown promising results for conventional anodizing process enhancing the corrosion resistance due to precipitation of the corresponding salt oxide/hydroxide products blocking the porosity [28]. Other good candidates are organic acid sealants in the form of organic solution, such as phosphonic acid, in which the improvement of the corrosion properties are due to the formation of a hydrophobic film on the coating surface and the plugging effect of micropores in the anodic coatings [28]. However suitability of these sealants for PEO coatings is not clear due to the complex composition and morphology of these coatings, including several types of aluminiun oxides, and only few works are reported. Barik et al. conducted investigations with PEO coated 6082 alloy and found a slight improvement in the corrosion behaviour after sol-gel sealing, but there was no improvement of the properties after sealing with sodium silicate [29]. Shrestha et al. [30] also achieved better corrosion properties after the application of sol-gel sealing on a commercial Keronite coating on AA2219 alloy, reaching 2000 hours in a salt spray test without corrosion attack. However, up to date there is no sealing method based on aqueous solutions able to improve significantly the corrosion properties of PEO coatings.

In the present study, PEO coatings are developed on A356 (gravity-cast and rheocast) aluminum alloys with a pre-anodized layer and different effects are evaluated in terms of characterization and corrosion behavior of the coated materials: i) the influence of the alloy manufacturing process ii) the effect of Si-rich phase on the structure and composition of the oxide layers iii) the corrosion behavior and the effectiveness of different sealing techniques based on salts of nickel, cerium, potassium permanganate and phosphonic acid.

2. Experimental

2.1. Material

Gravity-cast (A356-GC) and rheocast (A356-RC) aluminum alloys were manufactured by Cidaut (Spain) using a commercial A356 aluminum alloy with a theoretical liquidus temperature of 615 °C and binary eutectic temperature. The composition of the A356-GC alloy is wt.%: <0.001 Zn,0.0004 Sr, 0.0006 Mn, 6.83 Si, 0.153 Fe, 0.366 Mg, 0.144 Ti, 0.017 V, bal. Al and wt.%: <0.001 Zn, 0.015 Sr, 0.0006 Mn, 6.72 Si, 0.155 Fe, 0.369 Mg, 0.156 Ti, 0.018 V, bal. Al for the A356-RC. The alloys were cut into 20 × 17 × 3 mm coupons (A356-GC) and 1.5 mm-thick disks with a diameter of 35 mm (A356-RC), ground to P600 silicon carbide abrasive paper, rinsed in distilled water and isopropanol and dried in warm air. The working area of 1 cm^2 was defined using a stop-off Lacquer 45 (MacDermid plc).

2.2 Surface treatment based on anodizing techniques

The porous precursor films were formed on each alloy by pre-anodizing in sulfuric acid, using conditions described elsewhere [31].

After pre-anodizing PEO treatment was carried out in an electrolyte comprising 10.5 g/L water-glass ($(Na_2O(SiO_2)_x \cdot xH_2O$, ≥27% SiO_2, ρ=1.39 g/L) and 2.8 g/L KOH using a 2 kW regulated AC power supply (EAC-S2000, ET Systems electronic). A square waveform voltage signal was applied with a positive-to-negative pulse ratio of 490 V/-110 V at 50 Hz frequency and a current density limit of 500 mA/cm^2 (rms). Voltage-time and current-time dependencies were recorded using KUSB-3116 Keithley data acquisition card (500 kS/s). The treatment was stopped 600 s after the drop of the current was observed, i.e. at 1600 s and 1800

s of treatment for A356-GC and A356-RC, respectively, the typical current-time dependency can be found in [25].

2.3 Sealing post-treatments

Four different post-treatments were carried out by immersing the PEO coated specimens under the conditions described in Table 1. After that, all the samples were rinsed with isopropyl alcohol and dried in warm air.

2.4 Surface characterization

For metallographic characterization of un-coated materials, samples were wet ground through successive grades of silicon carbide abrasive papers from P120 to P600, followed by diamond finishing to 0.1 μm. Weck reagent (4 g potassium permanganate + 1 g sodium hydroxide + 200 mL deionised water) was used to reveal the constituents of the alloys. The cross-sections of the coated materials were prepared by grinding the specimens through successive grades of SiC abrasive paper, from P120 to P2000 followed by polishing with 1 μm diamond paste.

Samples were examined by both optical and scanning electron microscopy (SEM) using a JEOL JSM-6400 microscope equipped with Oxford Link energy dispersive X-ray (EDS) microanalysis hardware. EDS surface area analysis results are cited as an average of three measurements performed at different locations. Phase composition was examined by X-ray diffraction (XRD), using a Philips X'Pert diffractometer (Cu $K\alpha$ = 1.54056 Å) at a scanning speed of 0.01° per second for a scan range of 2θ from 10° to 80°.

Coating thicknesses were measured by the eddy current method, using a Fischer ISOSCOPE FMP10 portable instrument, taking the average of ten measurements with a standard deviation of ~0.5 μm and later confirmed with cross-sectional scanning electron microscopy (SEM).

Surface hardness of the PEO coated specimens was measured on polished cross-sections applying a load of 0.05 kg for 15 s using an AKASHI MVK-E3 Vickers microhardness machine. The cited values are the average of ten measurements. Roughness parameter *Ra* (arithmetic average of the absolute profile deviations within the scanning path) was obtained using a Surtronic 25 roughness tester (Taylor Hobson) and TalyProfile software applying a Gaussian filter of 0.4 mm. The presented values are the average of 5 measurements performed over a distance of 4 mm.

Static contact angles were measured in accordance with the sessile drop method using an FTA1000 Drop Shape Analysis System (First Ten Angstroms) and accompanying software. Measurements were performed using deionised water under ambient conditions (20-25 ºC, 30-35% relative humidity). Reported values are the averages of five measurements taken at different points.

2.5 Electrochemical measurements

DC and AC electrochemical measurements were performed using an AUTOLAB-PGSTAT 30 computer-controlled potentiostat in a naturally aerated 3.5 wt.% NaCl solution at room temperature (22 °C). A conventional three-electrode cell was used, employing a graphite

counter electrode, a silver–silver chloride reference electrode (SSE) with a potential of 0.210 V with respect to the standard hydrogen electrode (SHE) and the specimen as a working electrode with 1 cm^2 of exposed area. The solution concentration inside the reference electrode compartment was 3 M KCl.

Cyclic polarization measurements, DC measurements, were obtained after 1 h of immersion at a scan rate of 0.3 mV s^{-1}, from -300 mV to +2000 mV relative to the open circuit potential (OCP) and with a maximum current of 5 mA cm^{-2}. The corrosion potential (E_{corr}), corrosion current density (i_{corr}), pitting potential (E_{pit}) and repassivation potential (E_{rep}) were measured to evaluate the corrosion properties of the materials. E_{corr} and i_{corr} were derived from the potentiodynamic polarization curves after Tafel extrapolation. Fitting method to obtain these parameters can be found elsewhere [32]. Electrochemical impedance spectroscopy (EIS) or AC measurements, were also performed for immersion times ranging from 1 day to 28 days at room temperature (22 °C). A sinusoidal perturbation of 10 mV amplitude with respect to OCP and a frequency sweep from 0.01 Hz to 30 kHz was applied. Repeatability was tested by measuring at least three specimens. The impedance spectra were analyzed using ZView software, the goodness of fit of the spectra corresponded to chi-squared (square of the standard deviation between the original data and the calculated spectrum) values <0.01. The errors for the individual parameters of the equivalent electrical circuits (such as *CPE* and *R*) were <5%.

3. Results and discussion

3.1. Characterization of the porous precursor film

Fig. 1 and Fig. 2 show, respectively, the optical and backscattered scanning electron micrographs of the cross-sections of A356-GC and A356-RC alloys after conventional anodizing. The A356-GC (Fig. 1 (a,b)) has the typical microstructure of an hypoeutectic Al-Si casting alloy consisting of primary aluminum dendrites (α-Al) with Al-Si eutectic in the interdendritic spaces, silicon coarse flakes and intermetallic microconstituents. The A356-RC (Fig. 2 (a,b)) is characterized by fine and spherical particles of α-Al phase with the eutectic silicon and intermetallic compounds located in the interglobular regions. The microstructures of both alloys and the intermetallic phases were characterized in detail elsewhere [5].

For both alloys, the oxide layer seems to preserve the microstructure of the substrate, dendrites or globules depending of the manufacturing process. This significant influence of the microstructure is associated with the presence of secondary phases (eutectic Al-Si phases, and several intermetallics) that have a different behavior relative to the matrix during anodizing.

In particular, for the gravity-cast alloy (A356-GC) an oxide layer with an average thickness of (20.1±0.6) μm was developed with some irregularities due to the presence of second phase particles (Fig. 1 (a,b)). The presence of these phases at the substrate/oxide interface blocks the growth of the oxide film, showing a negative effect on the morphology of the porous anodic layer [22,24,32]. This detrimental influence can be observed in more detail for an AlFeSi intermetallic compound (Fig. 1 c) and for a silicon particle (Fig. 1 d). These heterogeneities are related to different factors: i) a change in the current distribution in favor of the aluminum matrix which is less resistive and ii) different rates of oxidation in comparison with the surrounding aluminum matrix. In the particular case of elemental silicon particles, there is an important influence of the formation of an anodic film (SiO_2); this phenomenon is only

possible under very high energy conditions (Si-O energy binding (466 kJ mol^{-1})) with a comparatively low Al-O energy binding (281 kJ mol^{-1}) and the process is characterized by a large oxygen gas generation that is trapped into the coating inhibiting the growth of continuous anodic film [34, 35].

Similar microstructural features were observed in the case of A356 RC alloy, where a non-regular thickness oxide layer with an average thickness of (20.7±1.8) μm was formed (Fig. 2 (a-d)). The different rates of anodizing of the secondary phases lead to a thinner oxide layer on the eutectic areas (~8 μm) than the oxide formed in the α-Al matrix (~25 μm). Due to the small size of the eutectic silicon particles in the interglobular regions (equivalent diameter of 1.8 ± 0.6 μm [5]) the oxide grows around the particle until it is completely entrapped in the layer, apparently causing no defects.

The absence of Al_2O_3 peaks in the XRD analysis indicates an amorphous nature of the coatings. Peaks of Si and Al are originating from the substrate and SiO_2 peaks are associated with the oxidation of eutectic silicon (Fig. 3).

3.2. Characterization of the PEO coatings

3.2.1. Morphology and composition

SEM plan views of PEO coatings on A356-GC and A356-RC alloys formed upon the porous precursor films are shown in Fig. 4 (a,b). The typical surface morphology of plasma electrolytic oxidation layers was observed, with pores and some micro-cracks on the surface at the sites of the discharge channels, due to the gas evolution through the molten oxide material during the PEO process and thermal stresses, respectively. The cross-sectional BSE

examination revealed relatively uniform coatings with a slight decrease of the thickness for the oxide layer over the eutectic areas (Fig. 4 (c,d)) and with an average thickness of (100±2) μm and (96±4) μm for A356-GC and A356-RC, respectively.

X-ray elemental mapping of A356-RC-PEO (Fig. 5) revealed that Al and O elements were homogeneously distributed throughout the coating thickness indicating the formation of Al_2O_3. An outer Si-rich layer (~12 at.%) of less than 30% of the coating thickness and an inner, denser layer composed of 40.65 at.% O, 52.65 at.% Al and 3.87 at.% Si, are observed. The same elemental distribution was found for the A356-GC-PEO showing ~16 at.% Si in the outer layer and a composition of 43.28 at.% O, 50.85 at.% Al and 3.46 at.% Si in the inner part of the coating. In addition, a slight enrichment of Si element can be observed in the oxide layer over the eutectic areas (Fig. 5d).

Fig. 6 shows the results of the XRD analyses on the PEO treated specimens. Both coatings consisted of a mixture of α-Al_2O_3, γ-Al_2O_3, SiO_2 and mullite ($3Al_2O_3 \cdot 2SiO_2$), the latter due to the high temperature of the microdischarges achieved during the coating process (>1400ºC) [36]. The presence of hard alumina phases (α-Al_2O_3, and mullite) are responsible of the good mechanical properties of the coating [10].

3.2.2. Microhardness

Cross-sectional microhardness results for A356-GC-PEO and A356-RC-PEO are shown as a function of the distance from the substrate-coating interface in Fig. 7. Hardness values for distances below zero correspond to indentations within the substrate material. For distances above zero, the results are in concordance with the typical microstructure of these coatings

showing higher values for the dense inner barrier and lower results for the porous outer layer [37]. The maximum values were 850 and 1000 HV for A356-GC-PEO and A356-RC-PEO, respectively, obtained at distances of 20 μm and 35 μm from the substrates. This difference in hardness is explained by the constituents of the coatings; further, the PEO treatment time for A356-RC was longer (due to the current drop was observed ~200 s later than for the A356-GC), i.e. the specimens were exposed to the microdischarges and high temperatures for longer time, which contributed to formation of hard alumina phases (α-Al_2O_3, and mullite) [10].

For comparison, the precursor layers exhibited 380±20 and 390±11 $HV_{0.025}$ for A356-GC and A356-RC, respectively. The high values obtained for the standard deviation in the case of the anodized and PEO layers (one order the magnitude higher than the bare material) are related with the irregularities in the anodized layer due to the presence of second phases particles and porosity.

3.3. Characterization of the PEO coatings with post-treatments

Table 2 shows the effect of the different post-treatments on the roughness and contact angle values of PEO coatings. The post-treatments did not influence the roughness of the PEO coatings. The contact angles of non-sealed PEO coatings correspond to highly hydrophilic surface, however they were undoubtedly affected by the surface porosity, as the coatings are highly absorbent. Nevertheless, the hydrophilic properties of the coatings are significantly decreased after the application of studied post-treatments. Decreased wettability is usually indicative of the improvement of corrosion properties [38].

For all cases with exception of SNi post-treatment, PEO coatings developed on the alloy A356-GC showed more hydrophobic properties than the rheocast alloy. This fact might be related to the differences on morphology and composition of the PEO coatings.

The highest value of contact angle was achieved for PEO coatings with octadecylphosphonic acid (ODPA) post-treatment (129±5° and 120±5° for A356-GC and A356-RC respectively), indicating hydrophobic behavior of these materials. Although sealing solutions containing permanganate and Ce decreased the hydrophilicity of the surface, contact angle values were still below 90°.

3.4 Electrochemical measurements

3.4.1 Potentiodynamic polarization curves

Fig. 8 (a) and 8 (b) show, respectively, the potentiodynamic polarization curves after 1h of immersion for A356-GC-PEO and A356-RC-PEO with and without post-treatments. The corresponding parameters derived from the potentiodynamic curves are listed in Table 3.

As shown in a previous study, for both untreated alloys, the corrosion process is under cathodic control (oxygen diffusion) and the repassivation potentials, E_{rep}, are below the E_{corr}, indicating favorable conditions for stable pit growth [5]. Nevertheless, the rheocast alloy typically shows lower corrosion current density than the gravity-cast alloy due to smaller potential differences between the constituents of the alloy.

PEO coated A356-GC-based materials with and without post-treatments showed corrosion current densities variations in the range of 1.4 $\times 10^{-5}$ and 8.0 $\times$ 10^{-5} mA/cm^2, whereas for coated A356-RC-based materials, values were between 1.7 $\times 10^{-5}$ and 4.2 $\times 10^{-5}$ mA/cm^2.

More significant differences were found in the E_{corr} values (Table 3) which may be attributed to several factors such as the morphology and composition of PEO coatings, the effectiveness of the sealing post-treatment and the hydrophobic properties of the surface. The permanganate-based sealing appears to be the most effective in terms of corrosion improvement of A356-GC-PEO (Fig 8 (a)), revealing the noblest E_{corr} (- 0.557 $V_{Ag/AgCl}$) and the largest passive area with a pitting potential of 0.13 $V_{Ag/AgCl}$. For A356-RC-PEO, the post-treatment based on nickel acetate solution showed the highest E_{corr} (-0.642 $V_{Ag/AgCl}$), however, it did not have a pronounced passive region and failed to repassivate, as E_{rep} was found to be much below the E_{corr}.

3.4.2 Electrochemical impedance spectroscopy

For the un-coated materials an extensive discussion about the impedance behavior in 3.5 wt% NaCl up to 28 d is found elsewhere [5]. In summary, the gravity-cast alloy exhibits active nucleation of pits after 1 day of immersion, whereas the rheocast alloy shows general corrosion. Likewise, for long immersion times the A356-RC alloy revealed a general uniform corrosion with high pitting resistance. This difference in behavior is related to the microstructure of the alloys and in particular to the surface potential of intermetallic particles.

Fig. 9 shows Nyquist and Bode diagrams the of the EIS experimental data for PEO coated materials with and without sealing post-treatments after 28 days of immersion in 3.5 wt.%

NaCl solution. The equivalent circuits used for simulation of the electrical parameters of the materials are shown in Fig. 10 and their corresponding electrochemical parameters are presented in Tables 4 and 5.

In the case of the non-sealed PEO coated materials, the experimental plot can be fitted to a nested equivalent circuit with two time constants ($CPE_{coat}R_{coat}$) and ($CPE_{dl}R_{ct}$), in series with the resistance of the electrolyte, R_e. CPE_{coat} and R_{coat} are the constant phase element representing capacitive behaviour of the coating and coating resistance. CPE_{dl} is the constant phase element of the double electric layer formed on the interface of the electrolyte and the inner poreless part of the coating; R_{ct} is the charge transfer resistance across it (Fig. 10(a)). Constant phase element reflects the heterogeneous nature of the oxide film, which behaves as a non-ideal capacitor and its impedance is expressed by the following equation;

$$Z = 1/[CPE\ (j\,\omega)^n]$$

Where ω i s radial frequency, n is the exponential factor ($-1 \leq n \leq 1$) and $j = \sqrt{-1}$ is the imaginary number. CPE corresponds to a numerical value of admittance of the system, 1/Z, at $\omega = 1$ rad s^{-1}. With n = 1, constant phase element becomes an ideal capacitor.

For all times of immersion the impedance values of the PEO-coated materials are substantially higher than that of the untreated substrates [5]. As for conventional anodizing, studies of corrosion resistance of anodic films on Al-Si cast alloys are scarce and are performed for immersion times much shorter than the shortest time used in this work (1 d). Therefore, direct comparison is not possible. For instance, for a 20 μm-thick hard anodized layer [40], R_p values obtained from polarization curves measured just after stabilization of the

system are understandably about 3 times higher than R_{ct} values for PEO coatings after 24 h of immersion obtained in this work (Table 4).

PEO coatings developed on pre-anodized A356-RC alloy show a higher coating resistance (R_{coat}) and charge transfer resistance (R_{ct}) comparing to the A356-GC-PEO (Table 4). Differences in the resistance values up to one order of magnitude confirm the better quality of the coatings developed in the rheocast aluminum alloy. This fact may be related to the better corrosion properties of the A356-RC compared to A356-GC due to [5]: i) reduction of the potential differences between Si/Fe intermetallics and the α-Al phase ii) refined morphology of Si particles in the A356-RC alloy may also promote the formation of a more homogeneous film passive film and the rapid repassivation of the bare metal. In addition, the longer time of exposure to microdiscarges and high temperatures (200 s more compared to A356-GC) for this material and the consequent formation of a higher amount of α-Al_2O_3 might also influence to this behavior.

The equivalent circuit used for sealed PEO coatings includes a finite length Warburg diffusion element (W_s) in series with the resistance of the coating (Fig. 10 (b)). W_s reflects transport limitations of corrosion-active species (Cl^-, Al^{3+}, OH^-, H^+) through the convoluted, "non-through" sealed pores of the coating and the presence of a resistance at the end of the diffusion path (i.e. the oxide film in the base of the pores exhibits resistive rather than capacitive properties) [39].

Nyquist and Bode plots (Fig. 9) reveal that the post-treatments have a beneficial effect, increasing the impedance and thereby reducing the susceptibility to corrosion. These results

are in concordance with the higher values of contact angles obtained after the post-treatments, confirming reduced permeability of the coatings by corrosive media [37]. Also, this improvement can be associated with an increase of the mass transfer limitation and diffusion resistance of the sealed pores that contribute to the total impedance of the coated material.

The surface appearance of the EIS tested coatings following 28 d immersion in naturally-aerated 3.5 wt.% NaCl solution (Fig. 11) revealed no signs of severe corrosion attack in any of the coatings. In particular, the material A356-RC-PEO showed no coating degradation as was expected from the higher R_{coat} values obtained in the impedance compared with the A356-GC-PEO.

The data in Table 5 are arranged in order of descending $Z_{0.01Hz}$ for 28 d of immersion for each alloy. The decrease of the resistance of the coating R_{coat} up to two orders of magnitude over the course of 28 days may be associated with the saturation of the coating pores with the electrolyte and the chemical degradation of the coatings.

The $Z_{0.01Hz}$ values for both PEO-coated alloys with different post-treatments indicate a strong relation between the morphology and composition of the coating and the efficiency of the post-treatments. In the case of the A356-GC-PEO the post-treatments based on permanganate and nickel acetate show better corrosion behavior with a W_s-R of 363.2 and 337.4 kΩ cm^2 respectively after 28 days of immersion in 3.5 wt.% NaCl solution. Whereas for the A356-RC-PEO the most effective post-treatment was based on ODPA, showing a resistance of the coating ~639 kΩ cm^2 after 28 days of immersion. The effectiveness of the post-treatment and

their stability in time may be related to the different composition and superficial properties of the PEO developed in pre-anodized A356 rheocast and gravity-cast alloys.

Figure 12 shows the cross sections of A356-GC alloy with PEO coatings and post-treatments based on permanganate and ODPA after immersion in naturally-aerated 3.5 wt.% NaCl solution for 28 d. These post-treatments were the best and the worst for A356-GC according to the electrochemical tests. None of the cross-sections revealed significant changes and no degradation was observed at the metal/coating interface. These results suggest that the differences found in the impedance values may be due to internal hydration processes inside the coating pores.

4. Conclusions

a) Anodized porous precursor film

1. The oxide layer preserves the microstructure of the substrate (positions of the intermetalics) depending of the manufacturing process.
2. The influence of the microstructure on anodizing is associated with the presence of secondary phases that have a different behavior relative to the matrix during anodizing.
3. The oxide layers are formed of amorphous Al_2O_3 and oxides of the eutectic phases.

b) PEO coatings on pre-anodized alloys.

1. PEO coatings consisted of a mixture of α-Al_2O_3, γ-Al_2O_3, SiO_2, and mullite ($3Al_2O_3 \cdot 2SiO_2$).

2. The current drop due to the increase in the coating impedance is delayed on A356-RC due to the lower uniformity of porous precursor film that affects the transition to the microdischarge regime (soft-sparking).

c) Corrosion behavior

1. The hydrophobic properties of the coatings improved after the application of the post-treatments.
2. Post-treatments have a beneficial effect increasing the coating impedance and thereby reducing the susceptibility to corrosion.
3. The potassium permanganate and nickel acetate-based sealings were the two most effective in terms of short and long term corrosion improvement of the A356-GC-PEO.
4. The post- treatment based on ODPA solution showed the best long term corrosion properties for A356-RC-PEO.

Acknowledgements

The authors are grateful to MICINN (Spain, MAT2012−38407-C03-02) for financial support.

M. Mohedano is grateful to the Alexander von Humboldt Foundation, Germany, for the award of AvH research fellowship and financial assistance. E. Matykina is grateful to the Ramon y Cajal Programme (MICINN, Spain, RYC-2010-06749).

References

[1] Z.X. Liang, B. Ye, L. Zhang, Q.G. Wang, W.Y. Yang, Q.D. Wang, A new high-strength and corrosion-resistant Al–Si based casting alloy, Mater. Lett. 97 (2013) 104-107.

[2] W.J. Tomlinson, S.J. Matthews, Cavitation erosion of aluminium alloys, J. Mater. Sci. 29 (1994) 1101-1108.

[3] S. Wisutmethangoon, S. Thongjan, N. Mahathaninwong, T. Plookphol, J. Wann, Precipitation hardening of A356 Al alloy produced by gas induced semi-solid process process, Mat: Sci. A-Struct. 532 (2012) 610-615.

[4] Z. Ma, A.M. Samuel, F.H. Samuel, H.W. Doty, S. Valtierra, A study of tensile properties in Al–Si–Cu and Al–Si–Mg alloys: Effect of β-iron intermetallics and porosity, Mat: Sci. A-Struct. 490 (2008) 36-51.

[5] R. Arrabal, B. Mingo, A. Pardo, M. Mohedano, E. Matykina, I. Rodríguez, Pitting corrosion of rheocast A356 aluminium alloy in 3.5 wt.% NaCl solution, Corros. Sci. 73 (2013) 342-355.

[6] Z Szklarska-Smialowska, Pitting corrosion of aluminum, Corros. Sci. 41 (1999) 1743-1767.

[7] J. Sykes, G.E. Thompson, D. Mayo, P. Skeldon, Anodic film formation on high strength aluminium alloy FVS0812, J. Mater. Sci. 32 (1997) 4909-4916.

[8] J. Sykes, G.E. Thompson, P. Skeldon, D. Mayo, Growth of porous anodic films on FVS0812 aluminium alloy, J. Mater. Sci. 33 (1998) 4159-4165.

[9] L.E. Fratila-Apachiei, F.D. Tichelaar, G.E. Thompson, H. Terryn, P. Skeldon, J. Duszczyk, L. Katherman, A transmission electron microscopy study of hard anodic oxide layers on AlSi(Cu) alloys, Electrochim. Acta 49 (2004) 3169-3177.

[10] A.L. Yerokhin, X. Nie, A. Leyland, A. Matthews, S.J. Dowey, Plasma electrolysis for surface engineering, Surf. Coat. Technol. 122 (1999) 73-93.

[11] E. Matykina, R. Arrabal, P. Skeldon, G.E. Thompson, Investigation of the growth processes of coatings formed by AC plasma electrolytic oxidation of aluminium, Surf. Coat. Technol. 54 (2009) 6767-6778.

[12] A. Curran, T.W. Clyne, Thermo-physical properties of plasma electrolytic oxide coatings on aluminium, Surf. Coat. Technol. 199 (2005) 168-179.

[13] A. Melhem, G. Henrion, T. Czerwiec, J.L. Briançon, T. Duchanoy, F. Brochard, T. Belmonte, Changes induced by process parameters in oxide layers grown by the PEO process on Al alloys, Surf. Coat. Technol. 205 (2011) 133-136.

[14] J.A. Curran, T.W. Clyne, The thermal conductivity of plasma electrolytic oxide coatings on aluminium and magnesium, Surf. Coat. Technol. 199 (2005) 177-183.

[15] L.O. Snizhko, A.L. Yerokhin, N.L. Gurevina, V.A. Patalakha, A. Matthews, Excessive oxygen evolution during plasma electrolytic oxidation of aluminium, Thin Solid Films, 516 (2007) 460-464.

[16] C.S. Dunleavy, J.A. Curran, T.W. Clyne, Time dependent statistics of plasma discharge parameters during bulk AC plasma electrolytic oxidation of aluminium, Appl. Surf. Sci. 268 (2013) 397-409.

[17] R.O. Hussein, X. Nie, D.O. Northwood, Influence of process parameters on electrolytic plasma discharging behaviour and aluminum oxide coating microstructure, Surf. Coat. Technol. 205 (2010) 1659-1667.

[18] E. Matykina, R. Arrabal, A. Mohamed, P. Skeldon, G.E. Thompson, Plasma electrolytic oxidation of pre-anodized aluminium, Corros. Sci. 51 (2009) 2897-2905.

[19] E. Matykina, R. Arrabal, P. Skeldon, G.E. Thompson, Optimisation of the plasma electrolytic oxidation process efficiency on aluminium, Surf. Interface Anal 42 (2010) 221-226.

[20] J. He, Q.Z. Cai, H.H. Luo, L. Yu, B.K. Wei, Influence of silicon on growth process of plasma electrolytic oxidation coating on Al–Si alloy, J. Alloy Compd. 471 (2009) 395-399.

[21] G. Sabatini, L. Ceschini, C. Martini, J.A. Williams, I.M. Hutchings, Improving sliding and abrasive wear behaviour of cast A356 and wrought AA7075 aluminium alloys by plasma electrolytic oxidation, Mater. Design. 31 (2010) 816-828.

[22] F. Xu, Y. Xia, G. Li, The mechanism of PEO process on Al–Si alloys with the bulk primary silicon, Appl. Surf. Sci. 255 (2009) 9531-9538.

[23] L.E Fratila-Apachitei, H Terryn, P Skeldon, G.E Thompson, J Duszczyk, L Katgerman, Influence of substrate microstructure on the growth of anodic oxide layers, Electrochim. Acta 49 (2004) 1127-1140.

[24] A. Forn, J.A. Picas, M.T. Baile, E. Martin, V.G. Garcia, Microstructure and tribological properties of anodic oxide layer formed on Al–Si alloy produced by semisolid processing, Surf. Coat. Technol. 202 (2007) 1139-1143.

[25] E. Matykina, R. Arrabal, A. Pardo, M. Mohedano, B. Mingo, I. Rodríguez, J. González, Energy-efficient PEO process of aluminium alloys, Mater. Lett. 127 (2014) 13-16.

[26] V.R. Capelossi, M. Poelman, I. Recloux, R.P.B. Hernandez, H.G. de Melo, M.G. Olivier, Corrosion protection of clad 2024 aluminum alloy anodized in tartaric-sulfuric acid bath and protected with hybrid sol–gel coating, Electrochim. Acta 124 (2014) 69-79.

[27] M. García-Rubio, M.P. de Lara, P. Ocón, S. Diekhoff, M. Beneke, A. Lavía, I. García, Effect of postreatment on the corrosion behaviour of tartaric–sulphuric anodic films, Electrochim.Acta 54 (2009) 4789-4800.

[28] L. Hao, R. Cheng, Sealing processes of anodic coatings: past, present and future, Met. Finish. 98 (2000) 8-18.

[29] R.C. Barik, J.A. Wharton, R.J.K. Wood, K.R. Stokes, R.L. Jones, Corrosion, erosion and erosion–corrosion performance of plasma electrolytic oxidation (PEO) deposited Al_2O_3 coatings, Surf. Coat. Technol. 199 (2005) 158-167.

[30] S. Shrestha, A. Merstallinger, D. Sickert, B.D. Dunn, Preliminary evaluation of black coating on AA2219 alloy produced by plasma electrolytic oxidation (PEO) process for space applications, ISMSE, (2003) 57-65.

[31] E. Matykina, R. Arrabal, P. Skeldon, G.E. Thompson, P. Belenguer, AC PEO of aluminium with porous alumina precursor films, Surf. Coat. Technol. 205 (2010) 1668-1678.

[32] M. Stern, A.L. Geary, Electrochemical Polarization I. A Theoretical Analysis of the Shape of Polarization Curves, J. Electrochem. Soc. 104 (1957) 56-63.

[33] R.N. Caron, J.T. Staley, in: G.E. Dieter (Ed.), Materials Selection and Design vol. 20, ASM Handbook, ASM International, Materials Park OH, 1997, p. 388.

[34] R. Arrabal, A. Pardo, M.C. Merino, M. Mohedano, P. Casajús, E. Matykina, P. Skeldon, G.E. Thompson, Corrosion behaviour of a magnesium matrix composite with a silicate plasma electrolytic oxidation coating, Corros. Sci. 52 (2010) 3738-3749.

[35] W. Xue, Q. Jin, Q. Zhu, M. Hua, Y. Ma, Anti-corrosion microarc oxidation coatings on SiCp/AZ31 magnesium matrix composite, J. Alloys Compd. 482 (2009) 208-212.

[36] S. Somiya, Y. Hirata, Mullite powder technology and applications in Japan, Ceramic Bulletin 70 (1991) 1624-1632.

[37] J.M. Wheeler, J.A. Curran, S. Sherstha, Microstructure and multi-scale mechanical behaviour of hard anodized and plasma electrolytic oxidation (PEO) coatings on aluminium alloy 5052, Surf. Coat. Technol. 207 (2012) 480-488.

[38] S.V. Gnedenkov, V.S. Egorkin, S.L. Sinebryukhov, I.E. Vyaliy, A.S. Pashinin, A.M. Emelyanenko, L.B. Boinovich, Formation and electrochemical

properties of the superhydrophobicna nocomposite coating on PEO pretreated Mg-Mn-Ce magnesium alloy, Surf. Coat. Technol. 232 (2013) 240-246.

[39] S.V. Gnedenkov, S.L. Sinebryukhov, V.I. Sergienko, Electrochemical impedance simulation of a metal oxide hetero structure/electrolyte interface: a review, Russ. J. Electrochem. 42 (2006) 197-250.

[40] X. Li, X. Nie, L. Wang, D.O. Northwood, Corrosion protection properties of anodic oxide coatings on an Al−Si alloy, Surf. Coat. Technol. 200 (2005) 1994-2000.

Tables

Figures

Fig. 1. Cross-section of A356-GC after conventional anodizing: a) Backscattered scanning electron micrograph (BSE), b) Optical micrograph, c) BSE detail of AlFeSi, d) BSE detail of Si.

Fig. 2. Cross-section of A356-RC after conventional anodizing: a) Backscattered scanning electron micrograph, b) Optical micrograph, c) Optical micrograph detail of Al-Si phase, d) BSE detail of AlFeSiMg.

Fig. 3. X-ray diffraction patterns of A356-GC and A356-RC aluminium alloys after conventional anodizing.

Fig. 4. Backscattered scanning electron micrograph of PEO coatings after conventional anodizing: a) Plan view A356-GC-PEO, b) Plan view A356-RC-PEO, c) Cross section A356-GC-PEO, d) Cross section A356-RC-PEO.

Fig. 5. X-ray elemental mapping of A356-RC-PEO: a) Mg, b) Al, c) O, d) Si.

Fig. 6. X-ray diffraction patterns of A356-GC and A356-RC aluminium alloys after PEO treatment.

Fig. 7. Cross-sectional microhardness results for A356-GC-PEO and A356-RC-PEO as a function of the distance from the substrate-coating interface.

Fig. 8. Potentiodynamic polarization curves after 1h of immersion for PEO coatings with and without post-treatments: a) A356-GC, b) A356-RC.

Fig. 9. Nyquist and Bode diagrams of the EIS spectra for uncoated and PEO coated materials with and without sealing post-treatments after 28 days of immersion in 3.5 wt.%NaCl solution.

Fig. 10. Equivalent circuits used for fitting of the electrical parameters of the materials: a) PEO coated materials b) PEO coated materials with sealing post-treatments.

Fig. 11. Surface morphology of EIS tested alloys after immersion in naturally-aerated 3.5 wt.% NaCl solution for 28 d: a) A356-GC-PEO, b) A356-GC-PEO-SNi, c) A356-GC-PEO-SCe, d) A356-GC-PEO-SP, e) A356-GC-PEO-SMn, f) A356-RC-PEO, g) A356-RC-PEO-SNi, h) A356-RC-PEO-SCe, i) A356-RC-PEO-SP, j) A356-RC-PEO-SMn.

Fig. 12. Cross-section micrograph (BSE) after immersion in naturally-aerated 3.5 wt.% NaCl solution for 28 d: a) A356-GC-PEO, b) A356-GC-PEO-SMn, c) A356-GC-PEO-SP.

Table1. Sealing post-treatment conditions.

Sealing post-treatment	Disolution	Temperature (°C)	Time (min)
SNi	6.8 g/L $NiAc_2 \cdot 4H_2O$, 5 g/L H_3BO_3, 10 g/L TEA	90	20
SCe	3 g/L $Ce(NO_3)_3$, 0.3 g/L H_2O_2, 1 g/L H_3BO_3	30	120
SP	0.1672 g/L Octadecylphosphonic acid in ethanol.	25	1440
SMn	8.6 g/L $Al(NO_3)_3$, 30 g/L $KMnO_4$	90	25

Table2. Roughness and contact angle values of PEO coatings with and without post-treatments.

Material	R_a (μm)	R_z (μm)	Contact angle (^{o})
A356-RC-PEO	2.5±0.3	11.0±1.0	10±3
A356-GC-PEO	2.6±0.2	11.4±0.5	42±8
A356-RC-PEO-SNi	2.66±0.04	11.4±0.2	36±5
A356-GC-PEO-SNi	2.56±0.15	11.2±0.7	22.8±1.9
A356-RC-PEO-SCe	2.6±0.3	11.3±1.0	74.6±1.0
A356-GC-PEO-SCe	2.5±0.3	11.2±1.1	87±3
A356-RC-PEO-SP	2.55±0.04	11.2±0.4	120±5
A356-GC-PEO-SP	2.75±0.16	11.9±0.5	129±5
A356-RC-PEO-SMn	2.4±0.2	10.7±0.7	54±10
A356-GC-PEO-SMn	2.58±0.11	11.2±0.4	80±15

Table 3. Parameters of the polarization curves after 1h of immersion for A356-GC-PEO and A356-RC-PEO with and without post-treatments.

Material	E_{corr} (V)	i_{corr} (mA/cm^2)	E_{pit} (V)	E_{rep} (V)
A356-GC	-0.635	8.11E-05	-0.605	-0.752
A356-GC-PEO	-0.898	5.20E-05	-0.419	-0.832
A356-GC-PEO-SNi	-0.634	8.05E-05	-0.44	-0.772
A356-GC-PEO-SCe	-0.808	1.40E-05	-0.429	-0.874
A356-GC-PEO-SP	-1.113	4.14E-05	-0.371	-0.803
A356-GC-PEO-SMn	-0.557	2.47E-05	0.135	-0.876
A356-RC	-0.705	9.21E-06	-0.652	-0.785
A356-RC-PEO	-0.909	4.20E-05	-0.616	-0.781
A356-RC-PEO-SNi	-0.642	4.01E-05	-0.549	-0.776
A356-RC-PEO-SCe	-1.111	3.27E-05	-0.501	-0.784
A356-RC-PEO-SP	-0.961	2.35E-05	-0.617	-0.793
A356-RC-PEO-SMn	-0.895	1.72E-05	-0.556	-0.798

Table 4. Fit parameters of the EIS equivalent circuits obtained for A356-GC and RC with PEO coatings up to 4 weeks of immersion in 3.5% wt NaCl.

Material	t	CPE_{coat} ($\mu S\ s^n\ cm^{-2}$)	n	R_{coat} ($k\Omega\ cm^2$)	CPE_{dl} ($\mu S\ s^n cm^{-2}$)	n	R_{ct} ($k\Omega\ cm^2$)	$Z_{0.01Hz}$ ($k\Omega\ cm^2$)
A356-GC-PEO	1d	5.4	0.75	5.54	48.6	0.92	47.4	52.7
	28d	20.2	0.78	11.9	53.5	0.77	57.6	55.3
A356-RC-PEO	1d	11.8	0.83	130.1	88.5	0.96	74.2	171.6
	28d	21.1	0.85	204.2	611.5	0.99	61.7	177.3

Table 5. Fit parameters of the EIS equivalent circuits obtained for A356-GC and RC with PEO coatings and sealing post-treatments up to 4 weeks of immersion in 3.5% wt NaCl.

Material	t	CPE_{coat} ($\mu S\ s^n\ cm^{-2}$)	n	R_{coat} ($k\Omega\ cm^2$)	W_s-R ($k\Omega\ cm^2$)	φ	W_s-T (s)	$Z_{0.01Hz}$ ($k\Omega\ cm^2$)
A356-GC -PEO-SMn	1 d	5.7	0.78	4.9	825.9	0.5	0.3	643.2
	28 d	12.0	0.84	2.2	363.2	0.6	0.7	306.1
A356-GC-PEO-SNi	1 d	5.6	0.83	687.0	269.6	0.75	31.4	623
	28 d	11.7	0.84	1.2	337.4	0.84	0.72	282.4
A356-GC -PEO-SCe	1 d	6.3	0.76	447.6	106.6	0.51	40.6	418.7
	28 d	17.5	0.84	308.8	125.7	0.83	70.9	280.4
A356-GC -PEO-SP	1 d	1.2	0.83	33.3	186.6	0.5	0.7	229.8
	28 d	11.8	0.79	2.0	274.9	0.85	1.1	226.5
A356-RC -PEO-SP	1 d	10.6	0.78	120.7	57.4	0.5	28.7	146.8
	28 d	19.5	0.78	638.9	92.1	0.66	32.2	316.4
A356-RC -PEO-SCe	1 d	4.8	0.78	21.7	1039.0	0.6	44.9	471.3
	28 d	15.1	0.71	2.9	383.3	0.68	1.9	248.6
A356-RC -PEO-SMn	1 d	10.7	0.70	1.2	211.8	0.6	0.8	185.3
	28 d	14.8	0.72	4.1	343.0	0.72	1.5	233.2
A356-RC -PEO-SNi	1 d	17.2	0.74	3.3	493.8	0.5	1.1	275.3
	28 d	18.3	0.74	0.9	320.6	0.63	2.0	218.5

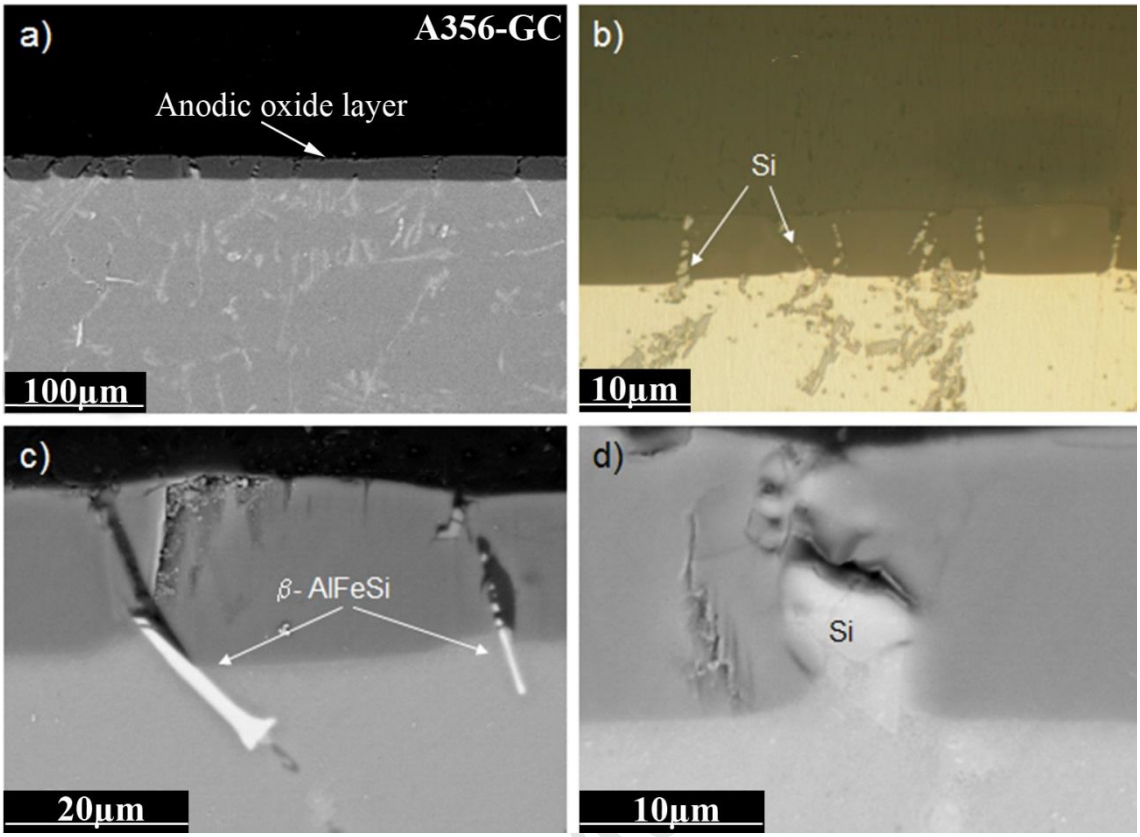

Fig. 1.

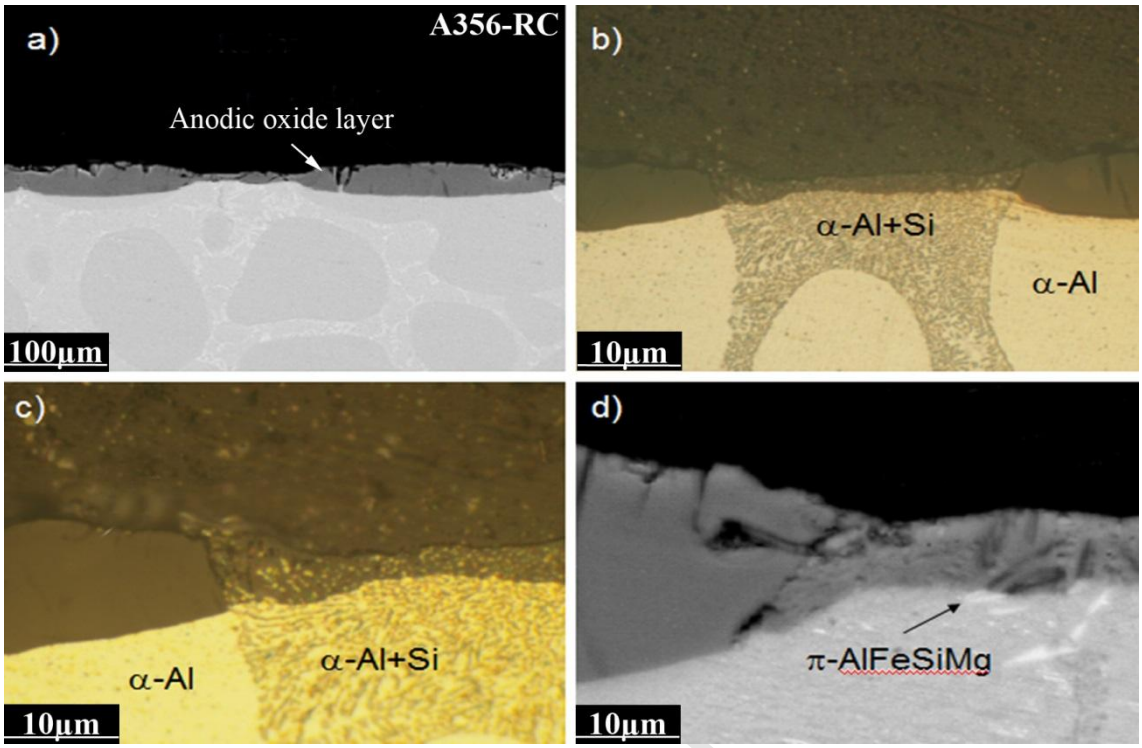

Fig. 2.

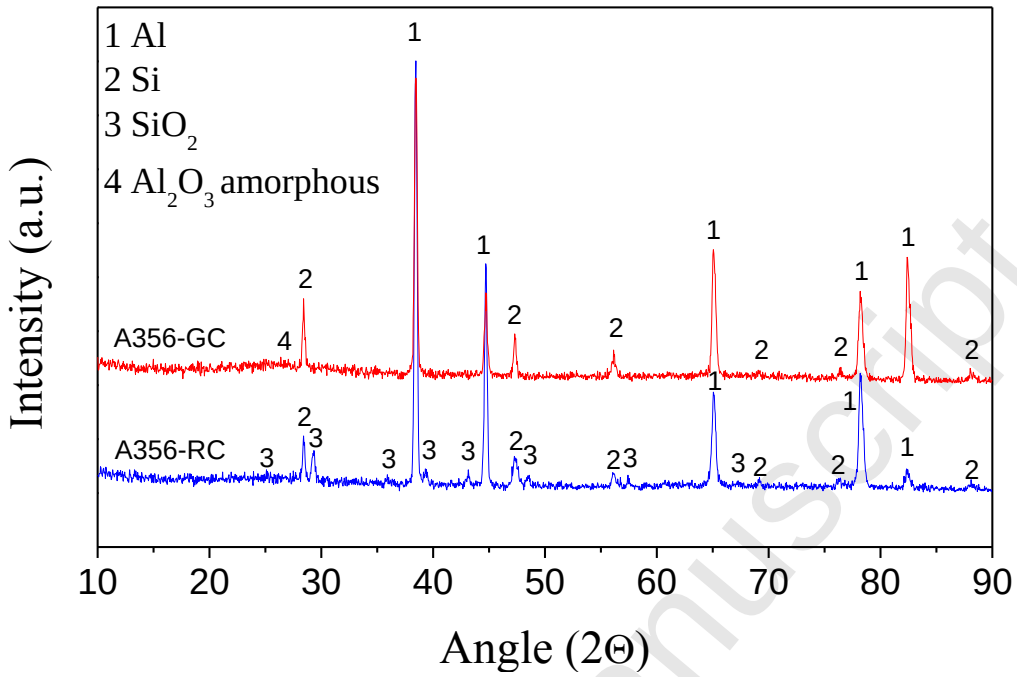

Fig. 3.

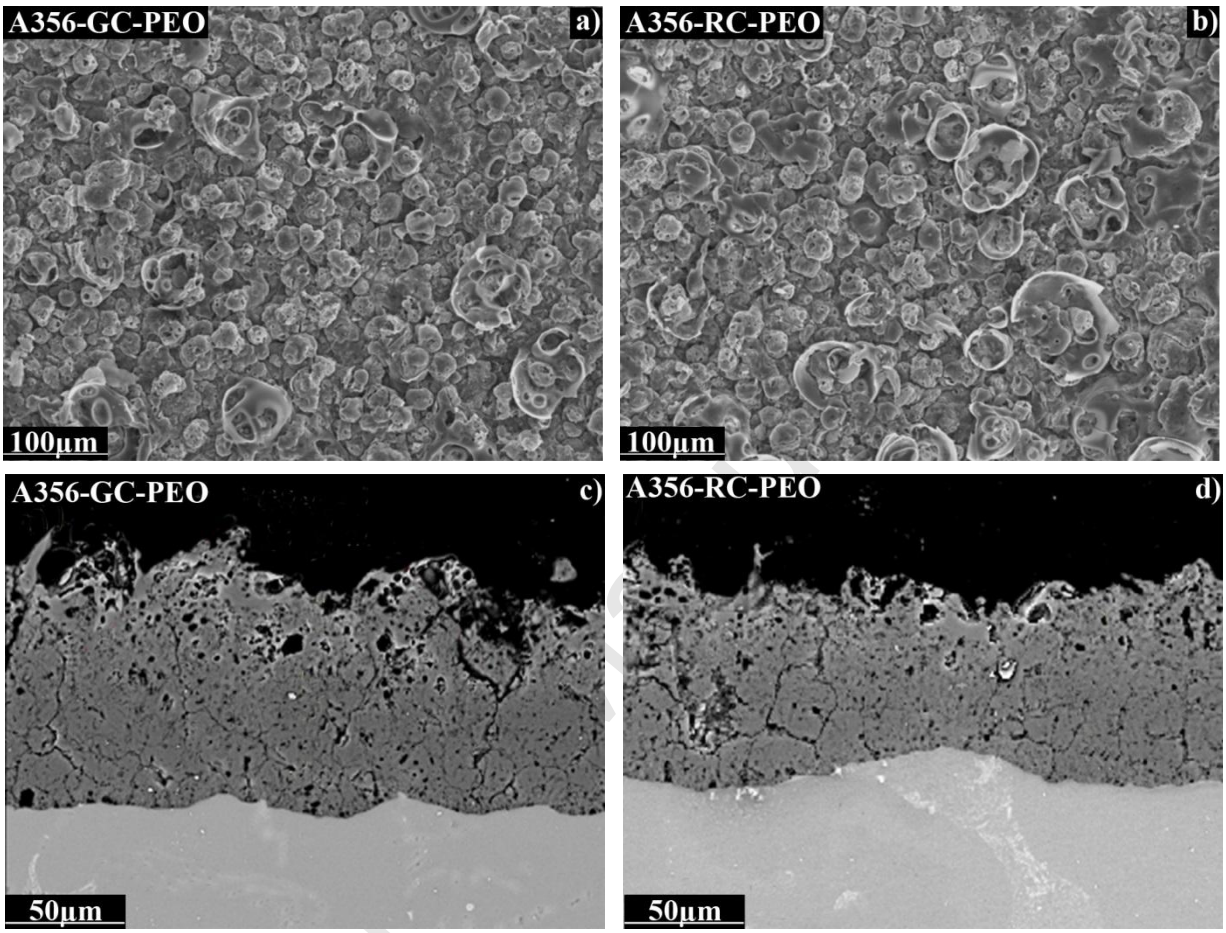

Fig. 4.

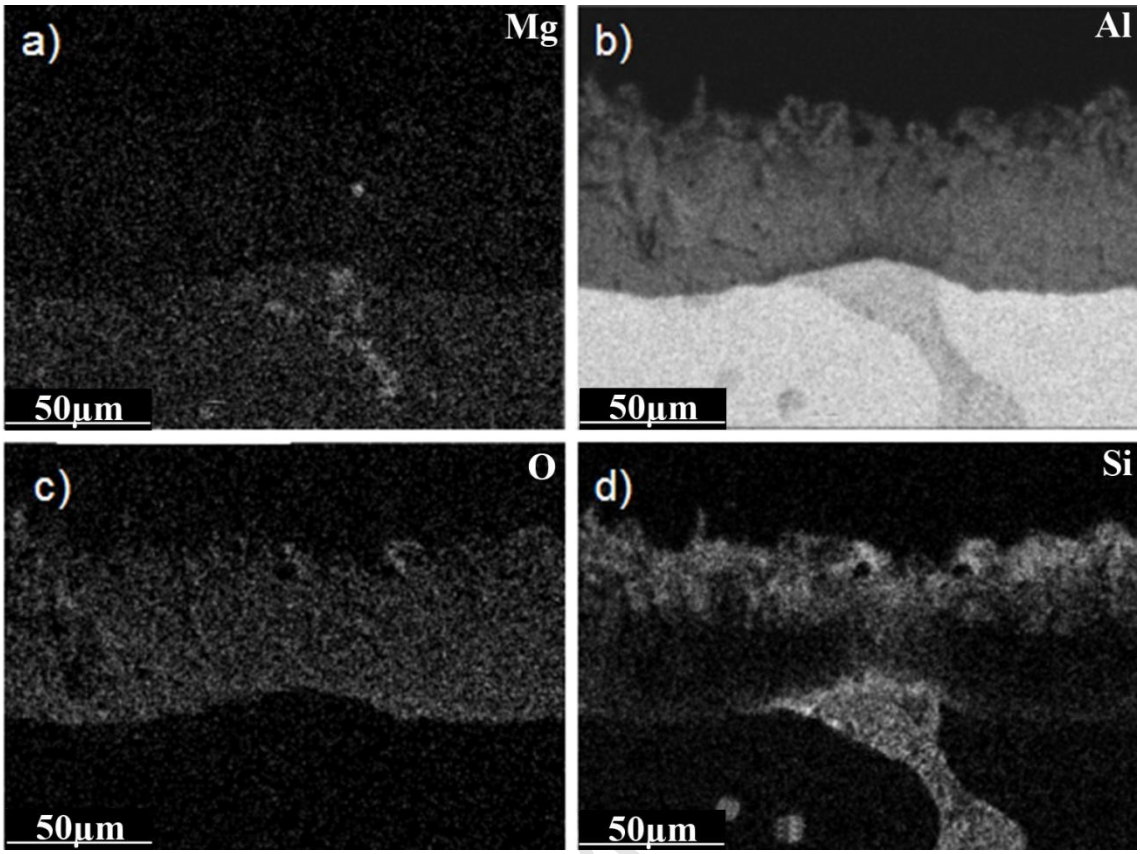

Fig. 5.

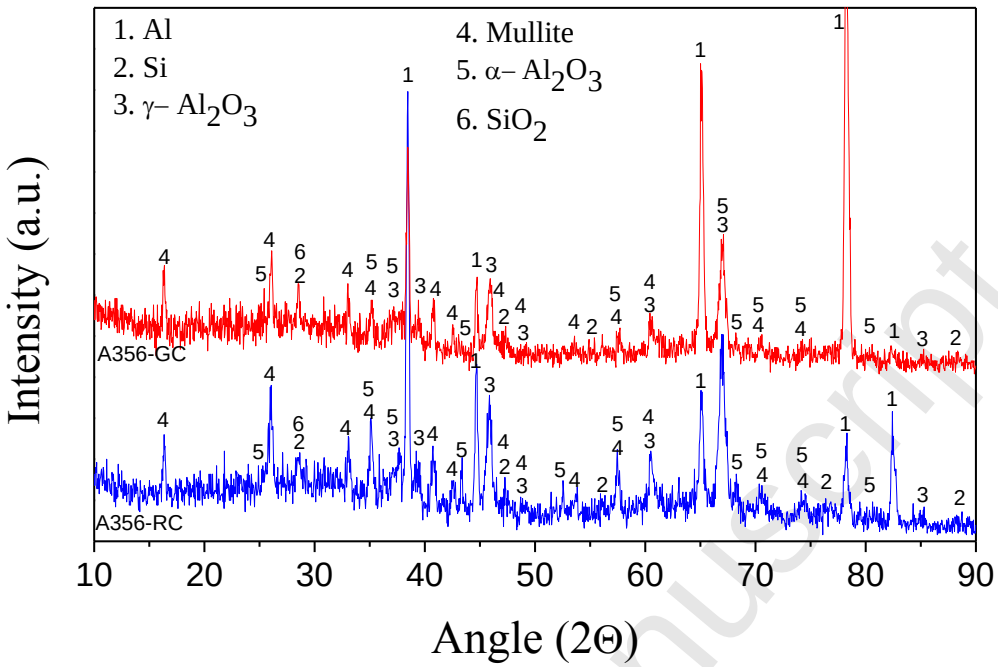

Fig. 6.

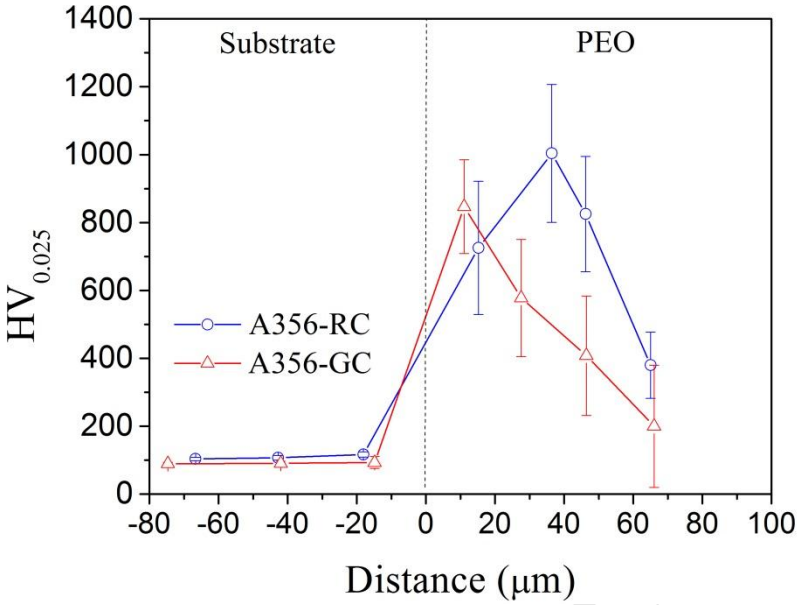

Fig. 7.

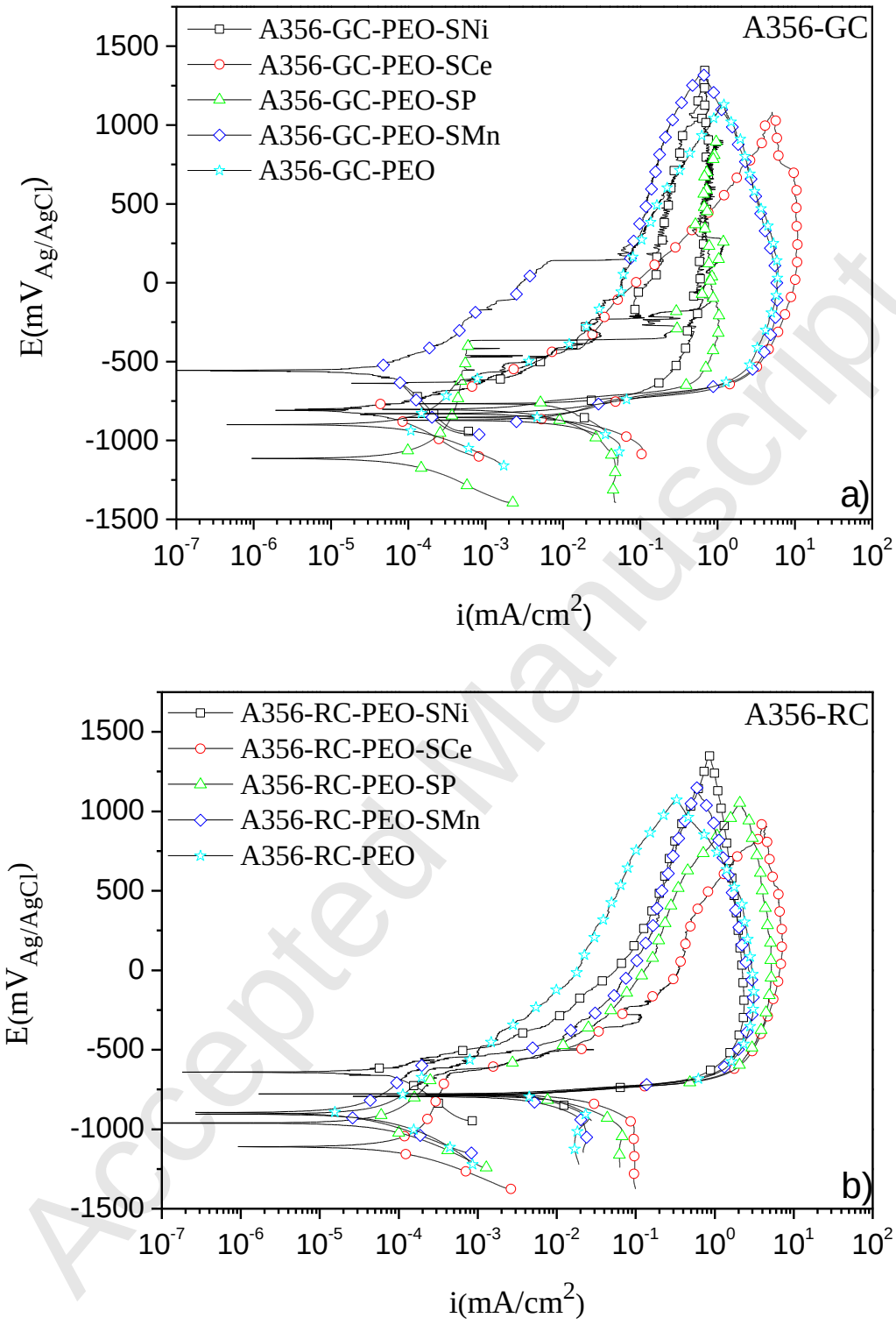

Fig. 8.

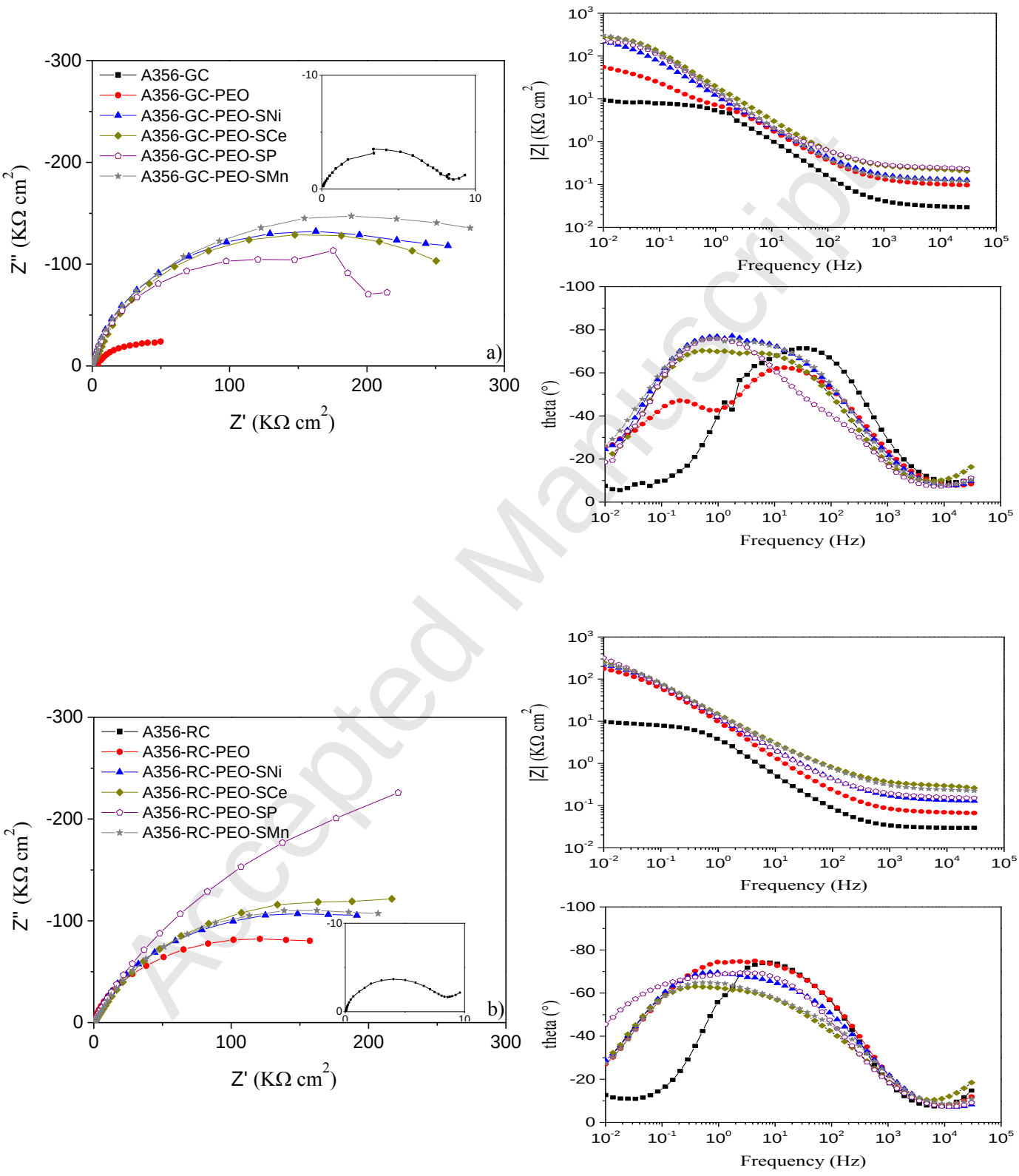

Fig. 9.

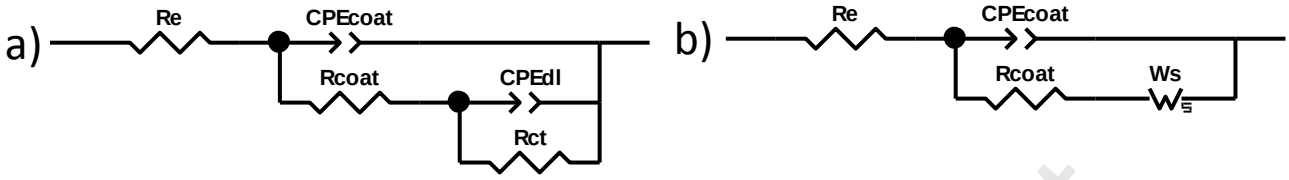

Fig. 10.

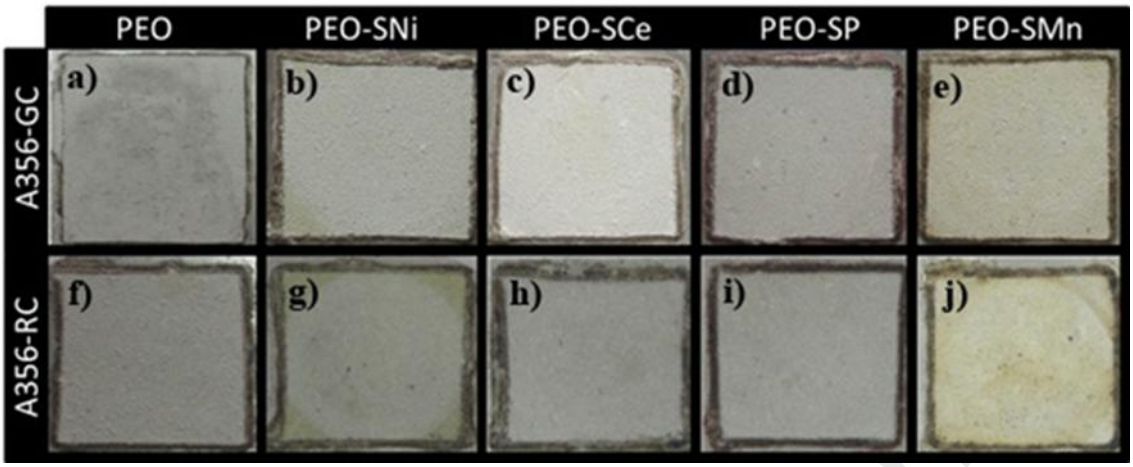

Fig. 11.

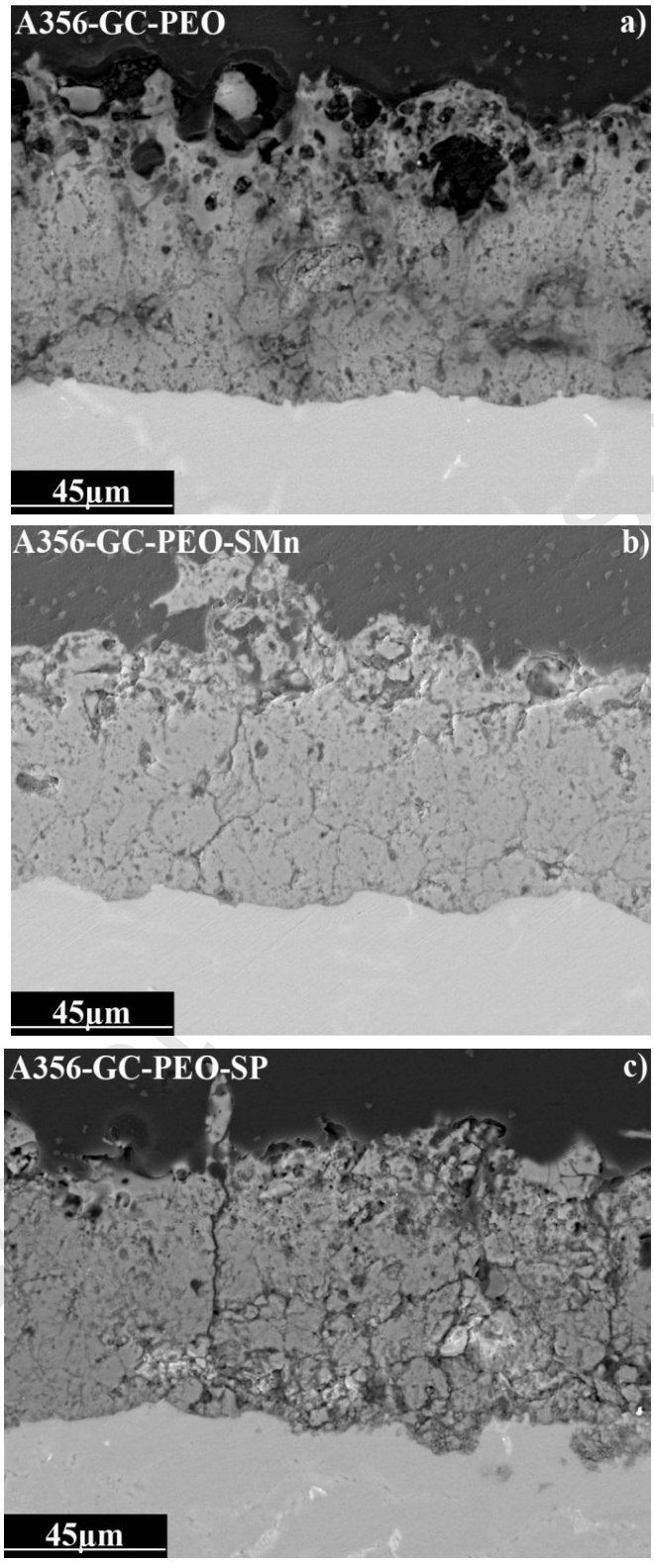

Fig. 12.